Research Article | Vol. 25, No. 12 | 12 Jun 2017 | OPTICS EXPRESS 13857
Optics EXPRESS

MHz frame rate hard X-ray phase-contrast imaging using synchrotron radiation

MARGIE P. OLBINADO,[1,*] XAVIER JUST,[2] JEAN-LOUIS GELET,[3] PIERRE LHUISSIER,[2] MARIO SCHEEL,[4] PATRIK VAGOVIC,[5,6] TOKUSHI SATO,[5,6] RITA GRACEFFA,[6] JOACHIM SCHULZ,[6] ADRIAN MANCUSO,[6] JOHN MORSE,[1] AND ALEXANDER RACK[1]

[1]*European Synchrotron Radiation Facility, CS40220, 38043 Grenoble Cedex 9, France*
[2]*Université Grenoble Alpes, Centre National de la Recherche Scientifique, Science Ingénierie des Matériaux et des Procédés, 38000 Grenoble, France*
[3]*MERSEN France SB, 15 rue Jacques de Vaucanson, 69720 Saint Bonnet de Mure, France*
[4]*Synchrotron SOLEIL, L'Orme des Merisiers Saint-Aubin, 91192 Gif-sur-Yvette, France*
[5]*Center for Free Electron Laser Science, Deutsches Elektronen-Synchrotron, Notkestrasse 85, 22607 Hamburg, Germany*
[6]*European X-ray Free Electron Laser GmbH, Holzkoppel 4, 22869 Schenefeld, Germany*
[*]*margie.olbinado@esrf.fr*

Abstract: Third generation synchrotron light sources offer high photon flux, partial spatial coherence, and ~10^{-10} s pulse widths. These enable hard X-ray phase-contrast imaging (XPCI) with single-bunch temporal resolutions. In this work, we exploited the MHz repetition rates of synchrotron X-ray pulses combined with indirect X-ray detection to demonstrate the potential of XPCI with millions of frames per second multiple-frame recording. This allows for the visualization of aperiodic or stochastic transient processes which are impossible to be realized using single-shot or stroboscopic XPCI. We present observations of various phenomena, such as crack tip propagation in glass, shock wave propagation in water and explosion during electric arc ignition, which evolve in the order of km/s (μm/ns).

OCIS codes: (110.7440) X-ray imaging; (170.6920) Time-resolved imaging; (340.6720) Synchrotron radiation; (110.2970) Image detection systems.

References and links

1. P. W. W. Fuller, "An introduction to high speed photography and photonics," Imaging Sci. J. **57**(6), 293–302 (2009).
2. L-3 Applied Technologies, Flash X-ray Systems, http://www2.l-3com.com/ati/solutions/irs_flash_x-ray.htm
3. F. Mizusako, K. Ogasawara, K. Kondo, F. Saito, and H. Tamura, "Flash x-ray radiography using imaging plates for the observation of hypervelocity objects," Rev. Sci. Instrum. **76**(2), 025102 (2005).
4. A. Momose, "Recent advances in X-ray phase imaging," Jpn. J. Appl. Phys. **44**(9A), 6355–6367 (2005).
5. A. Snigirev, I. Snigireva, V. G. Kohn, S. Kuznetsov, and I. Schelokov, "On the possibilities of x-ray phase contrast microimaging by coherent high-energy synchrotron radiation," Rev. Sci. Instrum. **66**(12), 5486–5492 (1995).
6. P. Cloetens, R. Barrett, J. Baruchel, J.-P. Guigay, and M. Schlenker, "Phase objects in synchrotron radiation hard x-ray imaging," J. Phys. D **29**(1), 133–146 (1996).
7. K. A. Nugent, T. E. Gureyev, D. J. Cookson, D. Paganin, and Z. Barnea, "Quantitative Phase Imaging Using Hard X Rays," Phys. Rev. Lett. **77**(14), 2961–2964 (1996).
8. J. A. Koch, O. L. Landen, B. J. Kozioziemski, N. Izumi, E. L. Dewald, J. D. Salmonson, and B. A. Hammel, "Refraction-enhanced x-ray radiography for inertial confinement fusion and laser-produced plasma applications," J. Appl. Phys. **105**(11), 113112 (2009).
9. J. Workman, J. Cobble, K. Flippo, D. C. Gautier, D. S. Montgomery, and D. T. Offermann, "Phase-contrast imaging using ultrafast x-rays in laser-shocked materials," Rev. Sci. Instrum. **81**(10), 10E529 (2010).
10. Y. Wang, X. Liu, K. S. Im, W. K. Lee, J. Wang, K. Fezzaa, D. L. S. Hung, and J. R. Winkelman, "Ultrafast X-ray study of dense-liquid-jet flow dynamics using structure-tracking velocimetry," Nat. Phys. **4**(4), 305–309 (2008).
11. J. S. Lee, B. M. Weon, S. J. Park, J. H. Je, K. Fezzaa, and W.-K. Lee, "Size limits the formation of liquid jets during bubble bursting," Nat. Commun. **2**, 367 (2011).

#291383 https://doi.org/10.1364/OE.25.013857
Journal © 2017 Received 24 Mar 2017; revised 12 May 2017; accepted 15 May 2017; published 9 Jun 2017

Optics EXPRESS

12. S. N. Luo, B. J. Jensen, D. E. Hooks, K. Fezzaa, K. J. Ramos, J. D. Yeager, K. Kwiatkowski, and T. Shimada, "Gas gun shock experiments with single-pulse x-ray phase contrast imaging and diffraction at the Advanced Photon Source," Rev. Sci. Instrum. **83**(7), 073903 (2012).
13. M. Hudspeth, B. Claus, S. Dubelman, J. Black, A. Mondal, N. Parab, C. Funnell, F. Hai, M. L. Qi, K. Fezzaa, S. N. Luo, and W. Chen, "High speed synchrotron x-ray phase contrast imaging of dynamic material response to split Hopkinson bar loading," Rev. Sci. Instrum. **84**(2), 025102 (2013).
14. A. Rack, F. García-Moreno, L. Helfen, M. Mukherjee, C. Jiménez, T. Rack, P. Cloetens, and J. Banhart, "Hierarchical radioscopy using polychromatic and partially coherent hard synchrotron radiation," Appl. Opt. **52**(33), 8122–8127 (2013).
15. D. E. Eakins and D. J. Chapman, "X-ray imaging of subsurface dynamics in high-Z materials at the Diamond Light Source," Rev. Sci. Instrum. **85**(12), 123708 (2014).
16. A. Rack, M. Scheel, L. Hardy, C. Curfs, A. Bonnin, and H. Reichert, "Exploiting coherence for real-time studies by single-bunch imaging," J. Synchrotron Radiat. **21**(4), 815–818 (2014).
17. A. Rack, M. Scheel, and A. N. Danilewsky, "Real-time direct and diffraction X-ray imaging of irregular silicon wafer breakage," IUCrJ **3**(2), 108–114 (2016).
18. A. Schropp, R. Hoppe, V. Meier, J. Patommel, F. Seiboth, Y. Ping, D. G. Hicks, M. A. Beckwith, G. W. Collins, A. Higginbotham, J. S. Wark, H. J. Lee, B. Nagler, E. C. Galtier, B. Arnold, U. Zastrau, J. B. Hastings, and C. G. Schroer, "Imaging Shock Waves in Diamond with Both High Temporal and Spatial Resolution at an XFEL," Sci. Rep. **5**(1), 11089 (2015).
19. A. Koch, "Lens coupled scintillating screen-CCD X-ray area detector with a high detective quantum efficiency," Nucl. Instrum. Methods Phys. Res. A **348**(2–3), 654–658 (1994).
20. A. G. MacPhee, M. W. Tate, C. F. Powell, Y. Yue, M. J. Renzi, A. Ercan, S. Narayanan, E. Fontes, J. Walther, J. Schaller, S. M. Gruner, and J. Wang, "X-ray Imaging of Shock Waves Generated By High-Pressure Fuel Sprays," Science **295**(5558), 1261–1263 (2002).
21. X. Liu, K.-S. Im, Y. Wang, J. Wang, M. W. Tate, A. Ercan, D. R. Schuette, and S. M. Gruner, "Four dimensional visualization of highly transient fuel sprays by microsecond quantitative x-ray tomography," Appl. Phys. Lett. **94**(8), 084101 (2009).
22. L. J. Koerner and S. M. Gruner, "X-ray analog pixel array detector for single synchrotron bunch time-resolved imaging," J. Synchrotron Radiat. **18**(2), 157–164 (2011).
23. H. T. Philipp, M. W. Tate, P. Purohit, K. S. Shanks, J. T. Weiss, and S. M. Gruner, "High-speed X-ray imaging pixel array detector for synchrotron bunch isolation," J. Synchrotron Radiat. **23**(2), 395–403 (2016).
24. T. Hatsui and H. Graafsma, "X-ray imaging detectors for synchrotron and XFEL sources," IUCrJ **2**(3), 371–383 (2015).
25. S. M. Gruner, D. Bilderback, I. Bazarov, K. Finkelstein, G. Krafft, L. Merminga, H. Padamsee, Q. Shen, C. Sinclair, and M. Tigner, "Energy recovery linacs as synchrotron radiation sources (invited)," Rev. Sci. Instrum. **73**(3), 1402–1406 (2002).
26. Th. Tschentscher, M. Altarelli, R. Brinkmann, T. Delissen, A. S. Schwarz, and K. Witte, "Technical Report: The European X-ray Free-Electron Laser Facility: A New Infrastructure for Research Using Ultrashort, Coherent X-ray Pulses of Extreme Brightness," Synchrotron Radiat. News **19**(6), 13–19 (2006).
27. ESRF Accelerator & Source Division "Characteristics of Beam Modes at the ESRF," http://www.esrf.fr/Accelerators/Operation/Modes
28. Photron Ltd, FASTCAM SA-Z, "Ultra High-Speed with Unprecedented Performance and Light Sensitivity," http://photron.com/high-speed/cameras/fastcam-sa-z/
29. T. G. Etoh, D. Poggemann, G. Kreider, H. Mutoh, A. J. P. Theuwissen, A. Ruckelshausen, Y. Kondo, H. Maruno, K. Takubo, H. Soya, K. Takehara, T. Okinaka, and Y. Takano, "An Image Sensor Which Captures 100 Consecutive Frames at 1 000 000 Frames/s," IEEE Trans. Electron Dev. **50**(1), 144–151 (2003).
30. Y. Tochigi, K. Hanzawa, Y. Kato, R. Kuroda, H. Mutoh, R. Hirose, H. Tominaga, K. Takubo, Y. Kondo, and S. Sugawa, "A Global-Shutter CMOS Image Sensor With Readout Speed of 1-Tpixel/s Burst and 780-Mpixel/s Continuous," IEEE J. Solid-State Circuits **48**(1), 329–338 (2013).
31. K. Miyauchi, T. Takeda, K. Hanzawa, Y. Tochigi, S. Sakai, R. Kuroda, H. Tominaga, R. Hirose, K. Takubo, Y. Kondo, and S. Sugawa, "Pixel Structure with 10 nsec Fully Charge Transfer Time for the 20M Frame Per Second Burst CMOS Image Sensor," Proc. SPIE-IS&T Electronic Imaging **9022**, 902203 (2014).
32. R. Kuroda, Y. Tochigi, K. Miyauchi, T. Takeda, H. Sugo, F. Shao, and S. Sugawa, "A 20Mfps Global Shutter CMOS Image Sensor with Improved Light Sensitivity and Power Consumption Performances," ITE Trans. MTA **4**(2), 149–154 (2016).
33. M. E. Rutherford, D. J. Chapman, T. G. White, M. Drakopoulos, A. Rack, and D. E. Eakins, "Evaluating scintillator performance in time-resolved hard X-ray studies at synchrotron light sources," J. Synchrotron Radiat. **23**(3), 685–693 (2016).
34. L. Pidol, A. Kahn-Harari, B. Viana, E. Virey, B. Ferrand, P. Dorenbos, J. T. M. de Haas, and C. W. E. van Eijk, "High Efficiency of Lutetium Silicate Scintillators, Ce-Doped LPS, and LYSO Crystals," IEEE Trans. Nucl. Sci. **51**(3), 1084–1087 (2004).
35. M. Nikl, "Scintillation detectors for x-rays," Meas. Sci. Technol. **17**(4), R37–R54 (2006).
36. M. Nikl, J. A. Mares, N. Solovieva, J. Hybler, A. Voloshinovskii, K. Nejezchleb, and K. Blazek, "Energy transfer to the Ce3+ centers in Lu3Al5O12:Ce scintillator," Phys. Stat. Solidi A **201**(7), R41–R44 (2004).

Optics EXPRESS

37. Z. Marton, V. V. Nagarkar, S. R. Miller, C. Brecher, H. B. Bhandari, P. Kenesei, S. K. Ross, J. D. Almer, and B. Singh, "Novel High Efficiency Microcolumnar LuI3:Ce for Hard X-ray Imaging," J. Phys. Conf. Ser. **493**, 012017 (2014).
38. G. Holst and T. S. Lomheim, *CMOS/CCD SENSORS and CAMERA SYSTEMS*, (SPIE Press, Winter Park FL and JCD Publishing, Bellingham, Washington, USA, 2007).
39. R. Kuroda, S. Kawada, S. Nasuno, T. Nakazawa, Y. Koda, K. Hanzawa, and S. Sugawa, "A Highly Ultraviolet Light Sensitive and Highly Robust Image Sensor Technology Based on Flattened Si Surface," ITE Trans. MTA **2**(2), 123–130 (2014).
40. A. Koch, C. Raven, P. Spanne, and A. Snigirev, "X-ray imaging with submicrometer resolution employing transparent luminescent screens," J. Opt. Soc. Am. A **15**(7), 1940–1951 (1998).
41. W. Chewpraditkul, L. Swiderski, M. Moszynski, T. Szczesniak, A. Syntfeld-Kazuch, C. Wanarak, and P. Limsuwan, "Scintillation Properties of LuAG:Ce, YAG:Ce and LYSO:Ce Crystals for Gamma-Ray Detection," IEEE Trans. Nucl. Sci. **56**(6), 3800–3805 (2009).
42. N. D. Parab, J. T. Black, B. Claus, M. Hudspeth, J. Sun, K. Fezzaa, and W. W. Chen, "Observation of Crack Propagation in Glass Using X-ray Phase Contrast Imaging," Int. J. Appl. Glass Sci. **5**(4), 363–373 (2014).
43. I. Schlichting, "Serial femtosecond crystallography: the first five years," IUCrJ **2**(2), 246–255 (2015).
44. Y. Tagawa, N. Oudalov, C. W. Visser, I. R. Peters, D. van der Meer, C. Sun, A. Prosperetti, and D. Lohse, "Highly Focused Supersonic Microjets," Phys. Rev. X **2**(3), 031002 (2012).
45. W. Bussière, "Electric fuses operation, a review: 1. Pre-arcing period," IOP Conf. Series: Materials Science and Engineering **29**, 012001 (2012).
46. W. M. Conn, "Combination of electrically exploded wires and electric arc," in *Conference on Extremely High Temperatures*, H. Fischer, L. C. Mansur, eds. (John Wiley & Sons, Inc., New York, 1958), p. 29.
47. A. Coulbois, P. André, W. Bussiere, J.-L. Gelet, and D. Rochette, "Spectroscopic study of the transition stage in fuse wire," XXth International Conference on Gas Discharges and their Applications, **1**(A46), 22–25 (2014).
48. X. Just, "Interaction entre arc et matière granulaire lors d'une coupure ultra-rapide dans un fusible," Ph.D. Dissertation, Université Grenoble Alpes, France (2016).
49. Princeton Instruments PI-MAX4 ICCD & emICCD, "The reference standard for time resolved imaging and spectroscopy," http://www.princetoninstruments.com/products/PI-MAX4-emICCD
50. pco. hsfc pro, "gateable MCP image intensifier for ultra short exposure times," https://www.pco-tech.com/highspeed-cameras/hsfc-pro/
51. S. Rutishauser, L. Samoylova, J. Krzywinski, O. Bunk, J. Grünert, H. Sinn, M. Cammarata, D. M. Fritz, and C. David, "Exploring the wavefront of hard X-ray free-electron laser radiation," Nat. Commun. **3**, 947 (2012).
52. A. P. Mancuso, Conceptual Design Report: Scienctific Instrument SPB, 2011.
53. R. Dimper, H. Reichert, P. Raimondi, L. S. Ortiz, F. Sette, and J. Susini, ESRF Upgrade Programme Phase II (2015 - 2022) Technical Design Study. http://www.esrf.fr/Apache_files/Upgrade/ESRF-orange-book.pdf
54. T. G. Etoh, A. Q. Nguyen, Y. Kamakura, K. Shimonomura, T. Y. Le, and N. Mori, "The Theoretical Highest Frame Rate of Silicon Image Sensors," Sensors (Basel) **17**(3), 483 (2017).
55. Z. Wang, C. L. Morris, J. S. Kapustinsky, K. Kwiatkowski, and S.-N. Luo, "Towards hard x-ray imaging at GHz frame rate," Rev. Sci. Instrum. **83**, 10E510 (2012).

1. Introduction

For decades, hard X-ray radiography based on attenuation-contrast has been the main approach employed to investigate transient processes, which evolve on timescales governed by material sound speeds in the order of km/s (μm/ns), in optically opaque objects. Ultra-high-speed (UHS) imaging has been realized using conventional flash X-ray systems with pulse widths of 10^{-7} to 10^{-9} s since the 1960s [1,2]. However, small density variations such as in spray jets [3] are difficult to visualize. Also, observations in low-density materials such as polymers and glasses are very challenging for X-ray radiography. These limitations on the sensitivity are overcome by X-ray phase-contrast imaging (XPCI), which relies on X-ray scattering cross sections which are up to three orders of magnitude larger than X-ray absorption cross sections [4]. Propagation-based XPCI [5–7] is mostly applied for real-time imaging of transient dynamics as it does not require any specialized optical elements that reduce X-ray photon flux. It has been adapted as a diagnostic for laser-induced-shock studies using laser-based backlighters, which generate 10^{-12} s width X-rays per flash, although with limited sensitivity due to spatial incoherence and low spectral brightness of the source [8,9].

At third generation storage ring (SR) synchrotron light sources, hard X-rays are available with high brilliance, ~10^{-10} s pulse widths and repetition rates up to several hundred MHz. High spatial coherence is inherent in low-emittance beams and enhanced by long-distance propagation from the source. In parallel with progress in X-ray detector instrumentation, UHS-XPCI using third generation synchrotron X-rays has become a rapidly developing field.

Optics EXPRESS

Dynamics in liquids and sprays, as well as fracture in a wide variety of materials including metals, polymers, and brittle materials such as glasses and ceramics have all been probed [10–17]. UHS imaging is defined as that employing 100 thousand frames per second (100 kfps) to 10 million frames per second (10 Mfps), or single-shot image acquisitions that employ exposure times of a hundred picoseconds to several microseconds [1]. We refer to exposure to a single synchrotron X-ray pulse as single-bunch imaging [12,13,16,17]. Alternatively, we refer to super-bunch or multiple-bunch imaging as the integration of a train of successive X-ray pulses, where the temporal resolution depends on the X-ray detector's exposure integration window; exposure times down to several hundred nanoseconds are frequently reached [10,11,14,15]. At the forefront, XPCI with unprecedented ~10^{-13} s temporal resolution and sensitivity using a fourth generation X-ray source based on the free electron laser (FEL) has been employed to visualize shock propagation in diamond [18].

High-sensitivity propagation-based XPCI relies on the availability of high spatial resolution hard X-ray imaging detectors. Reported UHS-XPCI using SR- and FEL-generated X-rays with spatial resolutions around 10 μm were successfully performed using the indirect X-ray detection scheme [10–18]. A scintillating screen is lens-coupled to a visible light camera which uses an imaging sensor (based on charged-coupled device (CCD) or complementary metal oxide semiconductor (CMOS) architectures) [19]. The optical beam path is necessarily folded at a 90° angle to prevent radiation damage to the optics, image sensor and electronics of the camera. Although direct detection schemes have been employed for UHS X-ray radiography [20,21] and have been reported for single-bunch isolation [22,23], the relatively large pixel pitch of these detectors does not meet the high-spatial resolution requirement of XPCI. Moreover, the frequently limited efficiency of silicon-based 'pixel detectors' for X-rays above 20 keV and the radiation damage that will result from exposure of the sensor to the intense beam have limited these detectors for applications to full-field X-ray imaging [24].

The MHz repetition rates of high-brilliance synchrotron X-ray pulses present enormous potential for UHS-XPCI. It allows the visualization of aperiodic and stochastic transient processes which are impossible to be visualized using just single-shot XPCI such as crack tip propagation, shock wave propagation in liquids or porous materials, high-speed jetting and spallation, and plasma explosions. X-ray pulses with MHz repetition rates are generated by storage ring synchrotron light sources as well as energy recovery linac (ERL) light sources [25] and the European XFEL [26] planned for future operations. In this work, we exploited the 1.4 MHz and 5.6 MHz X-rays of the European Synchrotron Radiation Facility (ESRF) and achieved up to 1.9 Mfps single-bunch XPCI for the visualization of crack propagation in glass and shock wave propagation in water. In addition, multiple-bunch XPCI with 5 Mfps was demonstrated using the uniform filling mode for the observation of explosions mediated by plasma arc expansion and metal vaporization during electric arc ignition. Multiple-frame video recordings with Mfps rates, large field of view and high spatial resolution were achieved by lens-coupling a burst CMOS camera with fast scintillators. The high temporal and spatial resolutions were achieved by carefully considering image lag, scintillator decay, spectral matching between the scintillator emission and image sensor spectral responsivity, scintillator thickness and numerical aperture of the coupling optical lens.

2. Experimental set-up

2.1 X-ray source

At SR synchrotron light sources, the maximum X-ray pulse rate is determined by the SR radio frequencies (RF), which are typically 352.2 or 500 MHz. At the ESRF the RF is 352.2 MHz and the maximum pulse rate is reached with the uniform filling mode involving 992 electron bunches circulating equidistant in the ring [27]. However, due to the limited total storage ring current the number of electrons in each bunch is scarce in the more densely populated filling

Optics EXPRESS

modes. For single-bunch imaging, we used the 4- and 16-bunch filling modes. With these modes, the increase in the number of X-ray photons per pulse, which scales linearly with the number of electrons per bunch, is achieved with a corresponding decrease in the bunch frequency as shown in Table 1. For multiple-bunch imaging, we used the uniform filling mode. With the currently available X-ray flux, we considered that the available X-ray photon statistics result in acceptable image quality for many investigations up to 10 Mfps. Note that an integration time of 80 ns in the uniform filling mode delivers the same number of photons as a single bunch in the 16-bunch filling mode. For the purpose of comparing the capabilities of various SR facilities for UHS imaging in terms of X-ray photon flux, a rough estimate can be made by comparing the electron charge per bunch of a given electron bunch filling mode of an SR facility. The actual X-ray photon flux for imaging will depend on the beamline, primarily on the type of its insertion devices.

Table 1. ESRF storage ring filling modes and the corresponding X-ray flux generated by U32 undulators at ID19 used for ultra-high-speed imaging.

filling mode	maximum ring current (mA)	bunch repetition (ns)	X-ray photons per pulse (10^6 photons/mm^2)
single-bunch	12	2816	44
4-bunch	40	704	37
16-bunch	90	176	20
992-bunch 'uniform fill'	200	2.84	0.7

Our experiments were performed at the X-ray microtomography beamline ID19 which is located 150-m from the source providing partially spatially coherent X-rays impinging on the sample. The beam was produced by two type U32 undulators operated with minimal gaps of 11.1 mm and 11.5 mm. The polychromatic beam energy spectrum exploitable for imaging ranges from ~20 keV to ~50 keV; the mean energy is ~30 keV. To reduce heat loads arising from beam absorption both in the sample and the scintillator screen, the beam was filtered by a 1.4 mm thick diamond window and 0.7 mm of aluminium, and X-ray exposures of the whole imaging system were limited to 200 ms by opening of a fast beam shutter during each video recording. The X-ray beam impinging on the sample was cropped by beamline slits to a size equal to the detector field of view.

2.2 X-ray detector

Using the indirect detector approach, multiple-frame video recordings for XPCI have been normally realized using conventional CMOS cameras which employ continuous image sensors. The high-speed readout of the camera could only be achieved by area of interest or sub-frame readout, i.e. with a reduction in the total number of sensor pixels used [11,13,14,16,17]. Mfps rates were thus achieved [28], but the field of view (FOV) and/or the spatial resolution have not been large enough to track the spatial evolution of many interesting dynamic phenomena. For example, a capture of a shock wave travelling in water at 1482 m/s requires a minimum FOV width of 1.5 mm with at least 1 Mfps.

In this work, we employed a burst image sensor which has pixel-based storage over multiple frames in order to achieve above 1 Mfps without reducing the total number of pixels in the image frame [29]. We used the UHS Hyper Vision HPV-X2 camera (Shimadzu Corp., Japan). In contrast with continuous image sensors, which read out every frame from the sensor immediately after its acquisition, a limited number of images is acquired at a frame rate in excess of the sensor's output bandwidth and stored in on-sensor memory for later "slow" read out [30]. UHS recording is achieved using 128 on-chip sensor memories giving 128 frames per burst video operation in full resolution mode (100 000 pixels) at a maximum frame rate of 5 Mfps. The sensor has 400 × 256 (250 effective) pixels of 30 µm × 21.3 µm active area at 32 µm pixel pitch, with a specified 10 000 electrons full well capacity. By the use of multiple implant regions, the pixel photodiode structure is optimized to transfer all the

Optics EXPRESS

photoelectrons from the photosensitive area of each pixel to its floating diode readout within 10 ns. The sensor memory architecture ensures that there is no image lag or "ghost" images resulting from preceding frames even down to 50 ns inter-frame time operation (i.e., 20 Mfps) [31,32]. The camera provides readout with a 10-bit analog to digital conversion (ADC) encoding and offers variable inter-frame times of multiples of 10 ns, enabling frame rates from 60 fps to 2 Mfps. The burst image acquisition sequence can be hardware triggered, but the image frame clock itself cannot be synchronized with an external clock, which is a serious limitation for synchrotron single-bunch X-ray imaging.

Equally important for achieving high-speed framing rates, large field of view, and high spatial resolution we considered the emission decay time of the scintillator screen material and its spectral matching to the sensor's quantum efficiency. Figure 1 shows the emission of various scintillators used for hard X-ray detection in the sub-microsecond regime which have been chosen using the criteria of high stopping power (X-ray attenuation length < 200 μm); light yield >20 photons emitted per keV X-ray energy absorbed; dominant decay times below 100 ns; and light emission wavelengths in the visible band rather than ultraviolet [33]. The scintillators are frequently single crystal Ce^{3+}-doped materials:

$$Y_3Al_5O_{12}\,(YAG):Ce;\ Lu_3Al_5O_{12}\,(LuAG):Ce;\ Gd_3Al_2Ga_3O_{12}\,(GAGG):Ce;$$
$$Cs_2NaYBr_3I_3\,(CNYBI):Ce;\ RdGd_2Br_7\,(RGB):Ce;\ LuI_3:Ce;\ YI_3:Ce;\ GdI_3:Ce;\ \text{and}$$
$$Lu_{2(1-x)}Y_{2x}SiO_5\,(LYSO):Ce.$$

In particular YAG:Ce; LuAG:Ce; and LYSO:Ce are considered as 'standard' scintillators as these are commercially available. Of these three, LYSO:Ce has the shortest decay, 38 ns, and shows negligible afterglow [34].

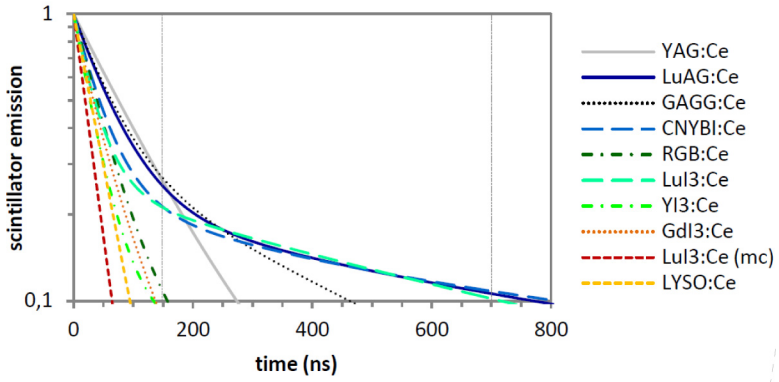

Fig. 1. Scintillator emission decay of various materials for hard X-ray detection on the sub-μs time scale. Note the log vertical scale. The curves were generated from decay constants gathered from literature presented in reference [33]. The dashed line cursors correspond to the 176 ns and 704 ns X-ray pulse repetition intervals of the 16- and 4-bunch ESRF operation modes used for single-bunch imaging.

Figure 2 shows the emission spectra of YAG:Ce, LuAG:Ce and LYSO:Ce scintillators and their matching to the spectral responsivity of image sensors used in high-speed cameras: HPV-X2 [32], Fastcam SA-Z (Photron Ltd., Japan), and pco.dimax (PCO AG, Germany). In general, the quantum efficiencies of most CCD and CMOS sensors fall off below 400 nm and above 800 nm [38]. From Fig. 2, YAG:Ce and LuAG:Ce with >50% of their emission between 500 nm and 600 nm are considered most compatible as regards spectral matching with the image sensors [35,36]. But the long lasting decay of these scintillators (as shown in Fig. 1) may cause image ghosting, which complicates quantitative image analysis in single-

Optics EXPRESS

bunch imaging. On the other hand, the fast scintillator LYSO:Ce has >50% of its emission between 380 nm and 450 nm, which is the low quantum efficiency region of the image sensors [34]. The quantum efficiency of image sensors in the blue-violet region needs to be improved, e.g. by thinning and backside illumination, so that the LYSO:Ce scintillator can be better implemented. As for the HPV-X2 CMOS sensor, its enhanced sensitivity to short wavelengths is achieved by optimization of the pixel sensitive area and photodiode junction fabricated on a near atomically flat Si surface [32,39]. We also note here a very promising scintillator which is not yet commercially available: micro-columnar (mc) LuI_3:Ce which has ~28 ns decay time, negligible afterglow, and peak emission between 450 nm and 600 nm [37]. In this work, single-crystal LYSO:Ce (Hilger Crystals, UK) and LuAG:Ce (Crytur, Czech Republic) of 250 µm thickness were used as scintillating screens.

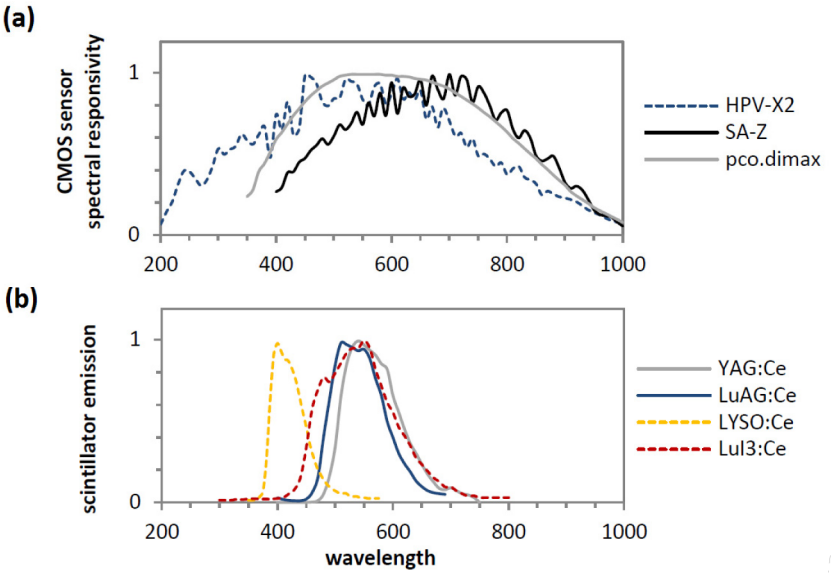

Fig. 2. (a) Normalized spectral responsivity as provided by the manufacturers for three image sensors used in high-speed cameras: Shimadzu HPV-X2 [32]; Photron Fastcam SA-Z; and the PCO pco.dimax camera. (b) Peak-intensity-normalized scintillator emission spectra of YAG:Ce [35]; LuAG:Ce [36]; LYSO:Ce [34]; and LuI_3:Ce [37].

An advantage of using indirect X-ray detectors is the adaptability of the optics according to the demand for larger FOV or higher spatial resolution: this is simply achieved by changing the (de)magnification of the optics. Take note, however, that image magnification comes at the price of a smaller number of photons reaching each image sensor pixel. To achieve the best image quality for a desired spatial resolution, we chose the numerical aperture (NA) and magnification of the objective lens which give the depth of focus that is compatible with the scintillator absorption depth at the photon energy used [40]. In this work, we used two lens systems: i) a 1 × optical magnification system comprising two Hasselblad lenses each of 100 mm focal length to exploit a large FOV of 12.8 mm × 8 mm and giving a nominal 32 µm effective pixel size, and ii) a custom fabricated lens assembly (Optique Peter, Lentilly, France) giving 4 × optical magnification to achieve higher spatial resolution with a 3.2 mm × 2.0 mm effective FOV and an 8 µm effective pixel size. For both systems, the objective lens NA was 0.2.

3. Evaluation of the X-ray detector

The sensitivity of the detector for ultra-high-speed X-ray detection was evaluated by measuring the decay curves of LYSO:Ce and LuAG:Ce scintillator emission generated from single-bunch synchrotron X-ray exposures. The 4-bunch filling mode of the ESRF was used.

Optics EXPRESS

The camera was operated with a frame rate that mismatched the arrival of the X-ray pulses by a few nanoseconds for each recorded frame, and we exploited this small mismatch to map the time structure of the scintillator emission decay. To capture X-ray pulses emitted from the same electron bunch, which occurs every 2816 ns (corresponding to the orbit period of the synchrotron storage ring) the inter-frame time of the camera was set to 2800 ns. The period mismatch between the X-ray pulse repetition and camera frame rate was 16 ns. Effectively, the camera exposure window of each frame slides away by 16 ns from the time of X-ray illumination, hence scans the scintillator decay. With this mismatch, the scintillator decay within 704 ns period is mapped within 44 frames. To evaluate the camera at a MHz frame rate, the inter-frame time was set to 710 ns. This corresponds to a 6 ns mismatch relative to the arrival of the pulses every 704 ns. In both measurements, the exposure time was 250 ns.

Figure 3 shows the temporal response of the LYSO:Ce and LuAG:Ce scintillator emissions as measured with the different camera systems. The measured LYSO:Ce emission decay curves confirm the absence of any significant afterglow: with a single exponential curve fit, giving an average decay time of $\tau = 34.2 \pm 2.8$ ns. The fitted time constant refers to the decay properties of the entire imaging system as measured with the HPV-X2 camera. A short decay time such as this has been previously reported and is suspected to result from the high heat load on the scintillator caused by the polychromatic X-ray beam irradiation [33,34]. Such high-sensitivity decay curve measurements obtained with indirect X-ray detection at a 1.4 Mfps recording rate has never been achieved before. Intensity scans such as these were previously performed using the PI-MAX 4 iCCD camera with several nanoseconds exposure times and at ~1 fps sampling rates [12,15,33].

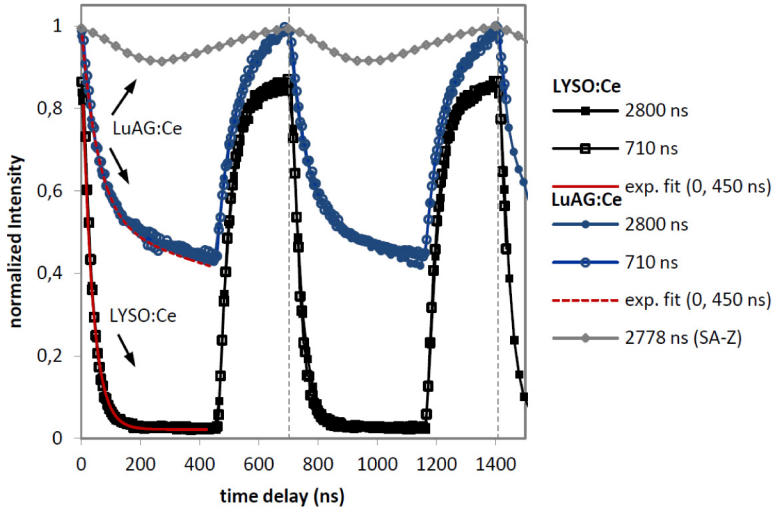

Fig. 3. Scans of the LYSO:Ce and LuAG:Ce scintillator emissions as a function of time delay with respect to single-bunch X-ray illumination. The response curves shown are for the burst image sensor camera HPV-X2 operated with inter-frame times 710 ns and 2800 ns and signal integration time of 250 ns. A response curve for the continuous image sensor (SA-Z) operated at 2778 ns and signal integration time of 248 ns with a LuAG:Ce scintillator is also shown. The dashed vertical lines indicate the 704 ns interval between X-ray pulses. The total dark noise was subtracted from each curve before normalizing the curves by their peak intensities. Each data point is an average intensity over a 50 × 50 pixels area. Exponential fits to the response curves using HPV-X2 for time delays 0 to 450 ns are also shown.

The LuAG:Ce emission decay curves were fitted with a double-exponential function which resulted in decay time constants of $\tau_1 = 57.4 \pm 2.4$ ns and $\tau_2 = 1967 \pm 157$ ns. The 250 ns exposures which integrated the scintillator emission after repeated X-ray illumination every 704 ns, resulted in a signal baseline shift corresponding to 40% of the peak intensity. In fact, trap centers in LuAG:Ce crystals result in multiple decay times [41], and this scintillator

Optics EXPRESS

must be employed with caution in time-resolved studies: the shift in the baseline signal is a sum of all previous X-ray pulse excitations, and correcting for this is not straightforward.

The sensitivity of the burst-type CMOS camera was also compared with one of the fastest CMOS cameras available in the market (Fastcam SA-Z, Photron Ltd., Japan) which uses a continuous readout image sensor. The SA-Z CMOS chip has 1024 × 1024 pixels of 20 μm size and is capable of frame rates up to 2.1 Mfps, but only with a reduced total number of pixels giving a frame size of 128 × 8. It claims a sensor 16 000 electrons full well capacity and dark noise of 29 electrons. One advantage of this camera for multiple-frame recording is its internal recording memory up to 64 Gbytes. The camera can be triggered and synchronized to an external clock, a highly desirable feature for single-bunch imaging. The SA-Z was operated at 2778 ns inter-frame time with an exposure time of 248 ns. Due to the poor spectral matching between LYSO:Ce and the SA-Z sensor as shown in Fig. 2, we could only use the Fastcam SA-Z with the LuAG:Ce scintillator.

The LuAG:Ce emission decay curve obtained using the Photron SA-Z camera operated with 2778 ns between frames is also shown in Fig. 3. Compared to the intensity scans of LuAG:Ce emission obtained with HPV-X2, the temporal response is far from the ideal exponential decay behavior with only a ~10% signal modulation obtained. This clearly shows the far higher effective sensitivity of using the HPV-X2 camera for single-bunch indirect X-ray detection at ultra-high-speed. The greatly improved sensitivity to the time structure of the X-ray pulses is attributed to the very high temporal resolution of the HPV-X2 camera, as evidenced by the absence of image lag even for 50 ns inter-frame time operation [31,32].

The spatial resolutions attained by the X-ray detector consisting of the HPV-X2 camera in combination with the two lens systems and 250 μm LYSO:Ce and LuAG:Ce scintillators were also measured using a standard X-ray test chart made of 0.05 mm lead foil between two 1 mm-thick plates of acrylic glass (Type 39, Hüttner Röntgenteste, Germany). We report the modulation transfer MT for a given spatial frequency f as the ratio of modulation M_f to that of a well-resolved spatial frequency $M_{reference}$, where the modulation depth M is given by $(I_{max} - I_{min})/(I_{max} + I_{min})$, I_{max} is the transmission through the glass and I_{min} is the transmission through the lead. The spatial resolutions were determined using the polychromatic beam generated by one U32 undulator at minimum gap. To determine the effect of the polychromatic illumination on the spatial resolution, measurements using a beam with peak energy ~19 keV and 1% bandwidth (using a U17-6 single-harmonic undulator) were also performed.

Figure 4 shows the X-ray transmission images of test charts used for spatial resolution measurements of the detector using combination of the 1 × and 4 × optical magnification systems with 250 μm thick LuAG:Ce and LYSO:Ce. For the purpose of comparison, the camera exposure times were chosen so that the signal-to-noise-ratio (SNR) for all images was 100, where “signal” is normalized X-ray transmission with a value of 1 and “noise” is the standard deviation. The spatial response of the detector using the 1 × and 4 × optical magnifications is dominated by aliasing effects related to the spatial sampling frequency, here with effective pixel sizes of 32 μm and 8 μm, respectively. On the left panel, the combination of the 1 × magnification lens system with LuAG:Ce and LYSO:Ce were able to resolve 16 line pairs per mm (LP/mm) with modulation transfers of 55% and 20%, respectively. On the right panel, the 4 × system combined with the same scintillators was able to resolve 20 LP/mm with modulation transfers of 80% and 70%, respectively. The 4 × system could resolve an edge (modulation depth = 1) within 2 pixels and no indication of smearing or tails to the intensity distribution. The smaller modulation transfers obtained with LYSO:Ce scintillator (both, 1 × and 4 ×) are attributed to the fact that the lenses are not optimized for the blue region. The effect was magnified with the 1 × system which was available off-the-shelf. We have not observed any difference in the spatial resolutions obtained between polychromatic and pink beam illumination. This indicates that the high energy components of the polychromatic illumination did not introduce detectable spurious scintillator emissions

Optics EXPRESS

due to Compton scattering. Such results may, however, be detected with higher magnifications.

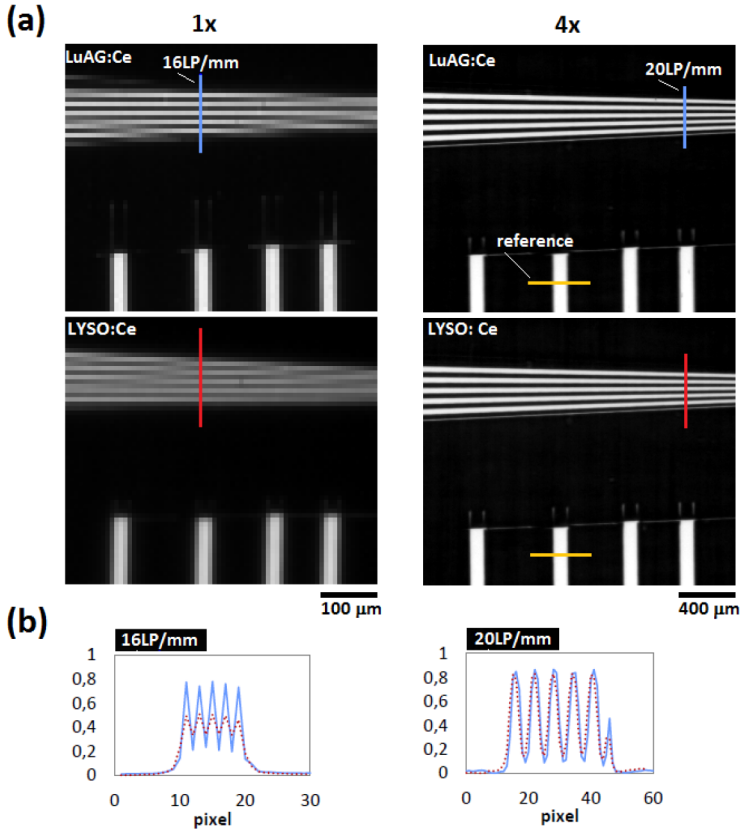

Fig. 4. (a) X-ray transmission images of test charts used for spatial resolution measurements of the detector using combination of the 1 × (left) and 4 × (right) optical magnification systems with 250 µm thick LuAG:Ce (top) and LYSO:Ce (bottom) scintillators. The images were normalized so that the modulation depth of the resolvable band M_{ref} is 1; grayscale: [0,1]. (b) Line profiles across f = 16LP/mm for the 1 × system, and f = 20LP/mm for the 4 × system.

4. X-ray phase-contrast imaging

Three visualizations are presented: 1) crack propagation in glass, for which a large FOV and single-bunch XPCI is necessary; 2) shock wave propagation in water, for which high resolution single-bunch XPCI was applied; and 3) explosion by plasma expansion during electric arc ignition occurring within a microsecond, where 5 Mfps multiple-bunch XPCI was used. Table 2 shows a summary of the X-ray imaging parameters.

Table 2. Summary of X-ray phase-contrast imaging parameters

Experiment	X-rays		HPV-X2 Camera		Scintillator	
	storage ring filling mode	pulse width (ps, rms)	inter-frame time (ns)	exposure time (ns)	thick -ness (µm)	material
Crack propagation	4-bunch	48	710	400	250	LuAG:Ce
Shock wave propagation	16-bunch	55	530	200	250	LYSO:Ce
Electric arc ignition	uniform		200	110	250	LuAG:Ce

Optics EXPRESS

4.1 Crack propagation in glass

The study of crack propagation in materials is important to understand material failure [42]. Crack propagation is an example of a dynamic phenomenon that cannot be precisely synchronized and is not repeatable; hence a UHS image detector with multiple-frame recording and large FOV is required. We used single-bunch XPCI with the ESRF 4-bunch filling mode taking advantage of the ultra fast X-ray pulses which 'freeze' the high-speed crack propagation [16]. The large FOV was achieved using the 1 × magnification lens system. The camera has no external frame clock synchronization capability; so the nearest inter-frame time of 710 ns (1.4 Mfps) provided by the internal camera clocking was used. Triggering of the mass free-fall used to initiate the crack was done using a pulse generator. The propagation distance between the sample and the detector was 6 m.

The time series observation of crack propagation in glass induced by the high-speed impact is shown in Fig. 5 (upper panel). Here, the clear depiction of the crack was achieved by X-ray phase-contrast edge enhancement at the crack interfaces: dark (bright) areas correspond to destructive (constructive) interference. The first evidence of a crack tip in the field of view (at time $t = 0$) is observed in the 100th frame, occurring 71 µs after the impact. At $t = 710$ ns, the crack tip has propagated as far as ~1200 µm, corresponding to an average speed of ~1.7 km/s. With the ~75 ps X-ray pulse, the motion blur at this speed of propagation is negligible (only 0.1 µm). This study is relevant to the ongoing efforts to visualize crack propagation [16], especially in Si wafers during breakage, which is a severe problem in semiconductor device manufacturing [17].

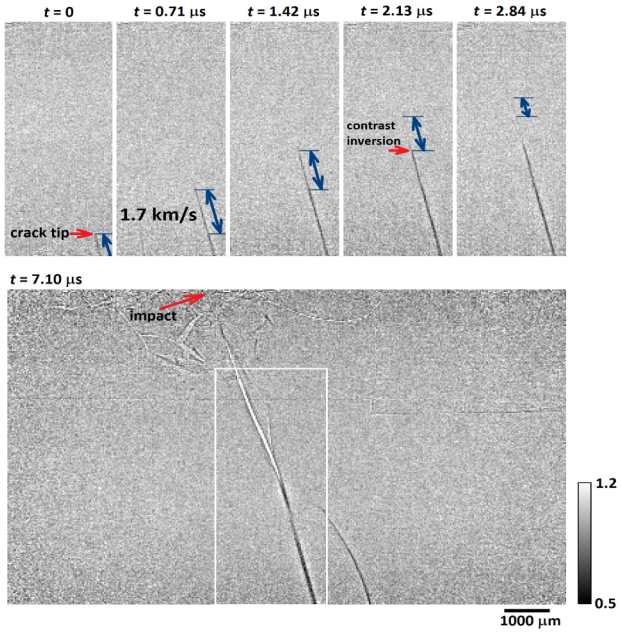

Fig. 5. Time series of single-bunch X-ray phase contrast images of crack propagation in glass observed with a camera operated at 1.4 Mfps (1/710 ns). The top panel shows the crack in the area of the glass within the white rectangle shown in the lower image. The crack is propagating upwards towards the impact point of the metal mass. The blue arrows indicate the incremental propagation of the crack between successive exposures. The grey scale indicated is normalized to the average background X-ray intensity transmitted through the glass. The image signal-to-noise-ratio (SNR) was 17.

Optics EXPRESS

4.2 Shock wave propagation in water

The visualization of shock wave propagation in materials using X-rays has been of huge interest for many scientists and engineers in order to understand material behaviour at the extreme conditions generated by high-speed impact [12,15,16] or laser ablation [9,18]. Although laser-induced shock is repeatable with high accuracy timing and synchronization, the stochastic process of shock propagation in liquids and porous materials is not fully captured in stroboscopic approach using single-shot X-ray imaging. In this work, we demonstrate the visualization of shock propagation in water as induced by pulsed nanosecond laser illumination. This study is an important aspect of sample delivery system instrumentation for serial femtosecond crystallography [43] at FEL facilities, wherein a pulsed sample injection can be achieved by laser-induced jetting of a liquid containing the samples for crystallography. Fluid dynamics are difficult to visualize using optical shadowgraphy due to the absorption of light in the liquid and multiple scattering by interfaces. Here we used single-bunch XPCI with the ESRF 16-bunch filling mode. The camera cannot be synchronized at the 5.6 Mfps rate required to capture X-ray pulses every 176 ns, so the camera was operated at an inter-frame time of 530 ns (1.9 Mfps) to capture every third X-ray pulse, i.e. every 528 ns. In order to achieve high spatial resolution the 4 × magnification objective lens system was used, and to increase the X-ray photon flux on the sample, the beam was collimated using ten X-ray compound-refractive lenses. A pulsed Nd:YAG laser (Minilite, Continuum) was used to induce the shock wave in a solution composed of water and Nile blue dye contained in an open-ended capillary sheet. The laser wavelength was 532 nm with a pulse duration 3 - 5 ns, and the attenuated laser beam energy was 2.03 mJ with a focal spot size of 300 µm. The 10 Hz laser flash lamp and q-switch operation were synchronised with the RF system using the BCDU8 unit and a delay generator-frequency divider (DG 645, Stanford Instruments). The sample-to-detector propagation distance which rendered most phase-enhanced contrast in the water was 1 m.

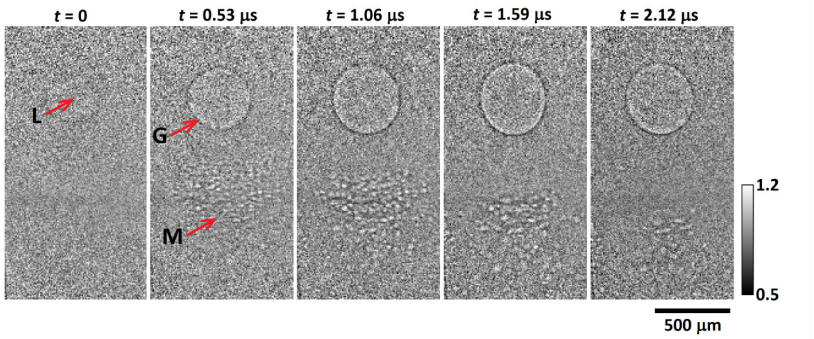

Fig. 6. Time series of single-bunch X-ray phase contrast images of laser-induced shock wave propagation in water observed with a camera operated at 1.9 Mfps (1/530 ns). The shock wave propagation was made evident by micro-cavitation seen as white speckles. The point of laser impact (L), expanding gas/ plasma (G), and propagating micro-cavitation (M) are indicated by red arrows. The grey scale indicated is normalized to the average background X-ray intensity transmitted through the liquid and glass. The image signal-to-noise-ratio (SNR) was 10.

Laser ablation in bulk water includes absorption, formation of plasma bubbles, and shock wave generation. A time series of XPCI of the laser-induced shock propagation in water is shown in Fig. 6. At t = 530 ns after the laser pulse hit the sample, micro-cavitation was seen as white speckles of 20 to 40 µm diameter, visible as far as 800 µm from the center of the laser impact. This corresponds to a speed of propagation of 1.5 km/s, confirming that a shock wave in water occurred and caused the micro-cavitation. This work is relevant to further the understanding of highly focused supersonic micro-jets, which were hypothesized to have been

Optics EXPRESS

induced by the impinging shock wave [44]. The 128 burst video recording that was achieved by the camera enabled tracking the evolution of the liquid dynamics such as bubble bursting, jet formation etc. following laser ablation.

4.3 Explosion by plasma expansion during electric arc ignition in a fuse

Explosion is another important dynamic phenomenon which exposes the dynamics of matter under extreme conditions. Here the explosion consists of the ejection of material mediated by the release of high energy densities transformed rapidly into heat and kinetic energy. The explosion resulting from the plasma expansion and metal vaporization that are generated during electric arc ignition in an electric fuse are phenomena that are not yet fully understood [45]. Fuses employ a ceramic case which is opaque to visible light, so hard X-ray imaging is necessary to visualize the melting and vaporization of the metal fuse strip during electric arc ignition. We applied multiple-bunch X-ray imaging using the ESRF uniform filling mode in order to provide enough X-ray photons for imaging with 110 ns exposure time at 5 Mfps. The 4 × magnification objective lens system was used for better spatial resolution, and to further increase the X-ray photon flux on the sample, the beam was collimated using 24 X-ray refractive lenses. A fuse was fabricated without its usual arc-quenching material (Mersen, France) to visualize the fundamental phenomena occurring during and immediately after electric arc ignition. The electric fuse operation was initiated by a high current delivered by a charged 8 mF capacitor and a gate turn-off thyristor switch. A pulse generator triggered both the electric fuse operation and the camera image acquisition, and an oscilloscope (Keysight Technologies, Canada) was used to monitor the fuse current and voltage across the fuse to confirm electric arc ignition. The sample-to-detector propagation distance was 3 m.

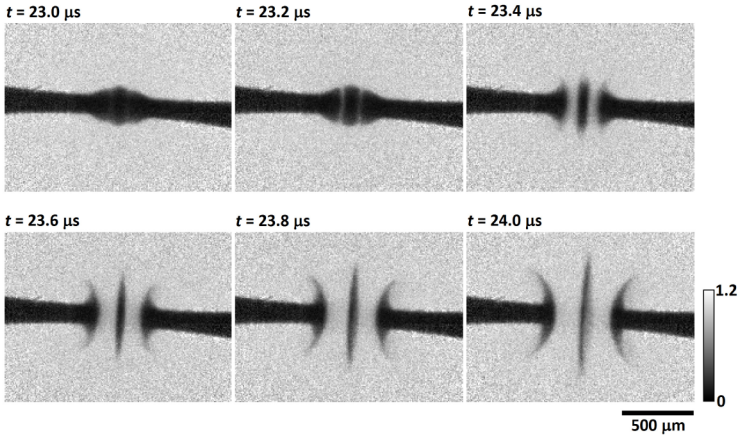

Fig. 7. Time series of X-ray radiographs of electric arc ignition (t = 23.0 µs to t = 24.0 µs) during fuse operation observed with 110 ns exposure time and at 5 Mfps. The radiographs are normalized by the X-ray intensity through the ceramic casing. The grey scale indicated is normalized to the average background X-ray intensity transmitted through the ceramic. The image signal-to-noise-ratio (SNR) was 13. (see Visualization 1)

A time series of X-ray radiographs during electric arc ignition of the electric fuse operation is shown in Fig. 7. The image contrast is mainly due to the difference in X-ray attenuation by the metal fuse strip, with a background level in the image determined by the partial X-ray transmission through the ceramic case. The radiographs reveal the melting of the silver metal strip, which starts at the constriction in the middle of the strip at time t ≈20.0 µs after the 'fault' current was generated to create Joule heating (see Visualization 1). At t = 23.0 µs, the exact time of occurrence of electric arc ignition was confirmed by the oscilloscope measurement of a sharp increase of voltage across the fuse. The electric arc ignition occurs with the appearance of plasma around the metal strip due to its partial vaporization at high

Optics EXPRESS

temperature [46]. The appearance of the striation after t = 23.0 µs is not exactly understood, but could be explained by Laplace magnetic forces acting on the liquid metal column due to the high current densities [47]. At t = 23.4 µs, an explosion occurs when the liquid metal is replaced by the arc plasma with estimated temperatures up to 20 000 K. These results show that the time series of images obtained between t = 23.0 µs and t = 24.0 µs are crucial in visualizing the striation which appears during electric arc ignition and which must be understood to properly formulate physical models of the fuse operation. Before this experiment, only "post-mortem" observations made on fuses using classic scanning electron microscopy and X-ray tomography were possible [48].

5. Discussion

As illustrated in our case studies, XPCI reveals instantaneous velocities and internal structures both in X-ray transparent materials such as glass and water, and inside optically opaque casing ceramic, which cannot be revealed by X-ray imaging based on attenuation-contrast alone and cannot be probed, or only partially probed, by conventional optical shadowgraph techniques. Combined with multiple-frame recording and MHz frame rates XPCI using synchrotron radiation and ultra-high-speed indirect X-ray image detection we were able to visualize, for the first time, crack tip propagation in glass, laser-induced shock waves in water and electric arc ignition. The visualizations that we have shown here will contribute to the validation of models for stochastic crack propagation; understanding laser-induced liquid-jetting, which is a candidate sample delivery system for serial femtosecond X-ray crystallography using FEL; and design specific electric fuses.

The multiple-frame recordings that were achieved are very relevant to dynamic studies that cannot be performed with a single-shot XPCI achieved using synchrotron radiation and laser-based backlighters. In the past, a time series of X-ray images at less than microsecond intervals without compromising the FOV has been achieved by repeating the experiments with varying time delays for each image acquisition [12,15,49]. This stroboscopic approach works well, though only if the experiment can be precisely timed and where it is possible to reproduce the experiment over many repetitions: in many cases however, information about dynamic evolution of materials has to be gathered in a single-shot experiment. Another solution has been to build optical multiplex combinations of several CCD cameras, which are triggered and synchronized with a high degree of precision [6,47,50]. However, this approach only works if the instantaneous X-ray photon flux is sufficiently high to be split with the (usually passive) optical multiplexing system and still yield sufficient photon statistics for each camera to provide an acceptable image quality.

In the context of real-time X-ray imaging instrumentation, the indirect imaging detector that we have developed sets a platform for development for other MHz frequency X-ray sources based on ERL [25] and FEL [26]. In particular, for the European XFEL Facility, which (will start its operation this year and unlike other hard X-ray FELs) will generate 4.5 MHz of femtosecond hard X-rays. For example, X-ray phase-contrast imaging of shock in diamond [18] could be performed in a single-experiment with MHz frame rate high spatial resolution image detection. Moreover, the multiple-frame recording X-ray detector with MHz frame rates and high spatial resolution (< 10 µm) that we have developed could be employed to perform pulse-to-pulse beam diagnostics of the femtosecond X-ray beam, and quantitatively derive the amplitude and phase information of the wavefront [51]. As the pulse-to-pulse position and energy spectrum of an FEL X-ray pulse considerably varies, diagnostics of the reference beam carried out at MHz frequency is essential for the correct quantitative X-ray phase retrieval necessary for X-ray phase imaging [18], serial femtosecond crystallography and coherent diffraction imaging applications [52] at the European XFEL.

The continuing developments in X-ray detection instrumentation is of great interest for the exploitation of synchrotron to X-ray imaging up to the ultimate frame rates set by RF frequencies of current storage rings (352 and 500 MHz). In particular, the upcoming upgrade

Optics EXPRESS

of the ESRF to an Extremely Brilliant Source (ESRF-EBS) based on a multi-bend achromat lattice design will deliver an increase of about two orders of magnitude in brilliance after year 2020 [53]. The 5 Mfps multiple-bunch XPCI that we have achieved with 110 ns exposures integrating the light from uniformly spaced single-bunches of 2.84 ns periodicity (352 MHz) gives us an idea that after the ESRF upgrade in 2020, a 40 × (110/2.84) increase in flux is enough to achieve GHz frame rate image acquisitions. On the other hand, prospects for Gfps frame rates for silicon image sensors have been put forward [54]. Close to the existing speed limits of CMOS electronics, schemes for GHz (picoseconds timing) hard X-ray imaging by indirect detection using a combination of fast scintillators with avalanche photodiode arrays of high-Z materials and micro-channel plate photomultipliers have also been reported [55].

6. Summary

We have demonstrated the high potential of the MHz repetition rates of high-brilliance synchrotron X-ray pulses for UHS-XPCI by visualizing aperiodic and stochastic transient processes which are impossible to be visualized using just single-shot XPCI such as crack tip propagation, shock wave propagation in liquid and plasma explosions. The visualizations of instantaneous velocities and internal structures during the evolution of a transient process inside X-ray transparent materials such as glass and water, and inside an optically opaque casing ceramic highlighted X-ray phase-contrast imaging as a powerful tool for diagnostics. We have developed a multiple-frame recording indirect X-ray detector capable of operating at up to 5 Mfps, offering a large field of view of 12.8 × 8 mm^2 and high spatial resolution with an effective pixel size of 8 μm. Recording at MHz frame rates without a reduction in the number of read-out pixels was achieved by employing a burst CMOS camera, and the large field of view or high spatial resolution were obtained using 1 × and 4 × optical magnification lens systems, respectively.

Funding

The French National Research Agency (ANR) EQUIPEX grant ANR-11-EQPX-0031 (project NanoimagesX).

Acknowledgments

We would like to acknowledge those who contributed during the experiments and the preparation of the manuscript: M. Morati and F. Balboni (MERSEN, France), A. Danilewsky (Albert-Ludwigs-Universität, Freiburg, Germany), M. Sikorski (European XFEL, Germany), A. Hovan and J. Ulicny (Pavol Jozef Safarik University in Kosice, Slovakia), V. Cantelli, E. Boller, P. Tafforeau and J.-P. Valade (ESRF, France), D. Bowley and W. Chan (Specialized Imaging, UK), M. Riches (Invisible Vision Ltd., UK), K. Tsuji (Shimadzu Europa GmbH, Germany), R. Kuroda (Tohoku University, Japan). D. Pelliccia (RMIT Univ. and Australian Synchrotron, Australia) and D. Paganin (Monash Univ., Australia) are acknowledged for the encouraging remarks and the help with the revision of the manuscript.